nature photonics

LETTERS

https://doi.org/10.1038/s41566-017-0089-9

Large optical nonlinearity of nanoantennas coupled to an epsilon-near-zero material

M. Zahirul Alam[1], Sebastian A. Schulz[1,2,3], Jeremy Upham[1], Israel De Leon[4*] and Robert W. Boyd[1,5]

The size and operating energy of a nonlinear optical device are fundamentally constrained by the weakness of the nonlinear optical response of common materials[1]. Here, we report that a 50-nm-thick optical metasurface made of optical dipole antennas coupled to an epsilon-near-zero material exhibits a broadband (~400 nm bandwidth) and ultrafast (recovery time less than 1 ps) intensity-dependent refractive index n_2 as large as -3.73 ± 0.56 cm^2 GW^{-1}. Furthermore, the metasurface exhibits a maximum optically induced refractive index change of ± 2.5 over a spectral range of ~200 nm. The inclusion of low-Q nanoantennas on an epsilon-near-zero thin film not only allows the design of a metasurface with an unprecedentedly large nonlinear optical response, but also offers the flexibility to tailor the sign of the response. Our technique removes a longstanding obstacle in nonlinear optics: the lack of materials with an ultrafast nonlinear contribution to refractive index on the order of unity. It consequently offers the possibility to design low-power nonlinear nano-optical devices with orders-of-magnitude smaller footprints.

All-optical signal processing and computation are often hailed as breakthrough technologies for the next generation of computation and communication devices. Two important parameters of such devices—energy consumption and size—critically depend on the strength of the nonlinear optical response of the materials from which they are made. However, materials typically exhibit an extremely weak nonlinear optical response. This property makes designing subwavelength all-optical active devices extremely difficult. Therefore, all-optical active devices tend to have large footprints, which limits the integration density to many orders of magnitude smaller than what can be achieved in state-of-the-art electronic integrated circuits[2,3]. Thus, materials with much stronger nonlinear optical responses are needed to enable integrated high-density on-chip nonlinear optical devices.

Over the years, several approaches have been explored to enhance the intrinsic nonlinear optical response of materials, including local field enhancement using composite structures[4–6], plasmonic structures[7,8] and metamaterials[9–12]. However, these techniques offer only limited control over the magnitude (and sign when applicable) of the wavelength-dependent nonlinear response, and typically involve a trade-off between the strength of the nonlinearity and the spectral position of the peak nonlinear response. It has been reported recently that materials with vanishingly small permittivity—commonly known as epsilon-near-zero or ENZ materials—exhibit intriguing linear[13–17] and large nonlinear responses[1,18–21]. However, an ENZ material has a large nonlinear response over only a relatively narrow spectral range. Furthermore, the zero-permittivity wavelength, strength of the nonlinear response, and losses depend on the optical properties of the ENZ material. In comparison to previous works[1,18] where strong nonlinear responses were reported in ENZ materials, here we show that many of these constraints can be overcome by incorporating engineered nanostructures on an ENZ host material. Specifically, we report a new approach to engineer an optical medium with an unprecedentedly large intensity-dependent refractive index using nanoantennas coupled to a thin ENZ material. The simple design concepts presented here provide exquisite control over engineering the sign and magnitude of the nonlinear refractive index, and can be used in an all-dielectric CMOS-compatible fabrication process to miniaturize nonlinear optical devices by orders of magnitude. We experimentally demonstrate that a metasurface geometry is uniquely suited to engineer a broadband and ultrafast nonlinear response orders of magnitude larger than those of any previously reported solid-state materials at optical frequencies.

The rationale for using a coupled ENZ–nanoantenna system as the building block for nonlinear optical devices is straightforward. Let us consider an optical antenna placed on a material exhibiting an intensity-dependent refractive index. A laser beam that is nearly resonant with such a system experiences a large effective linear refractive index. However, the resonance wavelength of a nanoantenna depends on its geometrical parameters and the refractive index of the surrounding medium. Thus, a small change in the refractive index of the substrate material leads to a spectral shift of the system's linear resonance as a consequence of the dynamic variation of the resonance wavelength of the nanoantenna. As a result, a high-intensity beam at a nearly resonant wavelength experiences a significantly different refractive index than that experienced by a low-intensity beam, as illustrated in Fig. 1, resulting in a large effective nonlinear refractive index change of the ENZ–nanoantenna system, Δn. Moreover, the field enhancement provided by the nanoantennas decreases the energy requirements for the nonlinear response. As a result, such a system can exhibit a broadband and large intensity-dependent refractive index.

We note that Δn can be either positive or negative, depending on the spectral position of the optical signal relative to that of the resonance at low intensity. Therefore, the sign, magnitude, wavelength position and bandwidth of Δn are no longer constrained by the ENZ substrate, but instead can be tailored by plasmonic or dielectric nanoresonators. These features make the system flexible enough to engineer both the magnitude and sign of the nonlinear response simply by engineering the linear dispersion, by appropriately choosing the antenna parameters and by choosing an ENZ host that exhibits the required nonlinear response[1,18].

We demonstrate the principle of operation using a metasurface[22–28] consisting of a two-dimensional array of gold optical

[1]Department of Physics, University of Ottawa, Ottawa, ON, Canada. [2]Centre for Advanced Photonics and Process Analysis, Cork Institute of Technology, Cork, Ireland. [3]Tyndall National Institute, Cork, Ireland. [4]School of Engineering and Sciences, Tecnologico de Monterrey, Monterrey, NL, Mexico. [5]Institute of Optics and Department of Physics and Astronomy, University of Rochester, Rochester, NY, USA. *e-mail: ideleon@itesm.mx

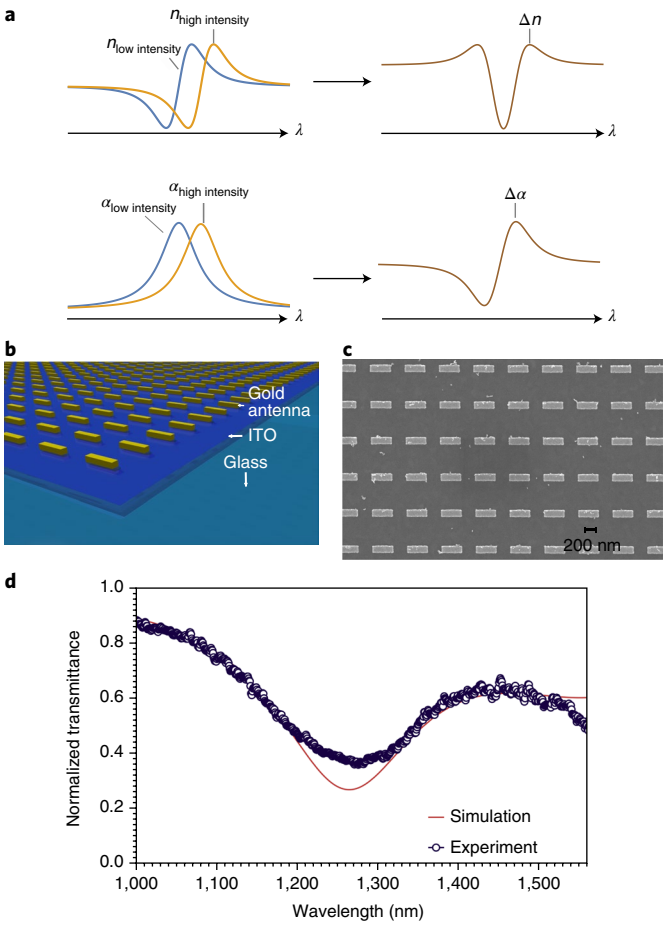

Fig. 1 | Design concept and linear response of the coupled structure. **a**, A small nonlinear change in the substrate material's refractive index results in a significant spectral shift of the resonance wavelength of an antenna. As a result, light of high intensity experiences a dramatically different refractive index (Δn) and a different absorption ($\Delta\alpha$) compared with those experienced by low-intensity light. **b**, The structure is composed of a gold dipole antenna array of 27 nm thickness on a glass substrate. A 23-nm-thick indium tin oxide (ITO) layer is sandwiched between the antenna array and the glass substrate. **c**, Scanning electron microscopy micrograph of the fabricated antenna array. **d**, The thin ENZ medium supports a bulk plasma mode near the zero-permittivity wavelength[30,43–45]. When a dipole antenna array with resonance at ~1,420 nm (due only to the presence of the glass substrate) is placed on an ITO–glass substrate, the transmission curve shows a splitting of the transmission resonance due to strong coupling between the fundamental mode of each antenna and the ENZ mode[31,32]. The variation between the experimental result and the FDTD simulation—with antennas of dimension 362 nm × 108 nm × 27 nm—can be attributed to inhomogeneous broadening of the linewidth of the antennas due to fabrication imperfections.

antennas on a thin ENZ layer, which in turn is deposited on a glass substrate (Fig. 1b). In this structure, an antenna plays three crucial roles: (1) it dictates the linear dispersion of the overall system, being responsible for a large effective refractive index at frequencies near-resonance; (2) it efficiently couples light at normal incidence to the ENZ layer; and (3) it provides a moderate optical field enhancement. We find that the interaction of the antennas with the ENZ layer simulatenously increases the refractive index change Δn for a constant incident intensity compared to the bare ENZ, and lowers the intensity threshold for the onset of the nonlinear response due to the moderate field enhancement inside the ENZ layer.

We used a 23-nm-thick film of indium tin oxide (ITO) as the ENZ layer. The real part of the permittivity of ITO crosses zero at $\lambda \approx 1{,}420$ nm. We chose the geometric parameters of the antenna such that its fundamental dipole resonance occurs at this wavelength. The thin ITO layer supports a lossy bulk-plasma mode at the zero-permittivity wavelength[29–31]. The linear optical transmission measurement of the metasurface (Fig. 1d) shows two distinct dips that result from the strong coupling-induced splitting between the fundamental mode of the antenna and the bulk-plasma mode of the ENZ layer. The coupled system exhibits two resonances, a main resonance centred at $\lambda = 1{,}280$ nm and a weaker resonance centred at $\lambda \approx 1{,}640$ nm. The wavelength separation between the resonances (~330 nm) is larger than the 3 dB linewidth of the antenna resonance on glass substrate alone (~30 nm)[31,32]. This strong coupling plays a significant role in the nonlinear response of the system.

We performed a series of Z-scan measurements[33] for various laser wavelengths to characterize the nonlinear response of the metasurface at normal incidence. We kept the incident intensity at the focus nearly constant at $I \approx 0.150$ GW cm^{-2} for all wavelengths. The polarization of the incident optical field was always along the long axis of the antenna. The metasurface exhibits both an intensity-dependent refractive index and an intensity-dependent absorption. The former is characterized by the effective nonlinear refractive index, $n_2 = \Delta n/I$, and the latter by the effective nonlinear absorption coefficient, $\beta = \Delta\alpha/I$, where Δn and $\Delta\alpha$ are, respectively, the changes in the effective refractive index and in the effective absorption resulting from illuminating the medium with an incident intensity of I. The results are shown in Fig. 2a,b. We find that the nonlinear response is strongly enhanced across the entire spectral range of interest, $1{,}180\ \text{nm} \leq \lambda \leq 1{,}560$ nm. The sign and magnitude of the nonlinear parameters depend on which side of the linear resonance is under investigation, and can be reproduced using a semi-quantitative numerical model describing the redshift of the linear dispersion of the coupled structure caused by the positive-valued intensity-dependent refractive index of ITO (see Supplementary Section 'Two-temperature model').

The metasurface displays a feature-rich and wavelength-dependent nonlinear response that can be used to control both the magnitude and the sign of the nonlinear parameters. The measured n_2 (Fig. 2a) show extremely large values at the negative ($\lambda = 1{,}240$ nm) and positive ($\lambda = 1{,}300$ nm) peaks, associated with the main resonance of the system. The absolute maximum response $|n_2| = 3.73 \pm 0.56$ cm^2 GW^{-1} is almost 2,000 times larger than the maximum n_2 of the bare 23-nm-thick ITO at $\lambda = 1{,}400$ nm (see Supplementary Section 'Nonlinear response of ITO') and is three orders of magnitude larger than that of a recently reported highly nonlinear metamaterial[19]. The magnitude of n_2 decreases steadily as a function of increasing wavelength ($\lambda > 1{,}300$ nm). Nevertheless, even at a red-detuned wavelength ($\lambda = 1{,}480$ nm), the nonlinear index, $n^2 = 0.589 \pm 0.088$ cm^2 GW^{-1}, is six orders of magnitude larger than that of silica glass and over two orders of magnitude larger than the nonlinearity of a high-conductivity ITO film at the ENZ region at normal incidence[1]. Similarly, the measured values of β (Fig. 2b) have a positive or negative sign depending on the optical wavelength. The values of β for $\lambda < 1{,}250$ nm and $\lambda > 1{,}440$ nm are negative, indicating saturable absorption, whereas the values for $1{,}250\ \text{nm} < \lambda < 1{,}440$ nm are positive, indicating reverse saturable absorption. The absolute maximum value of β is a factor of three smaller than that of a highly nonlinear metamaterial made of structured plasmonic metamolecules[11]. Alternatively, one could design the antenna array in a way to exhibit a much larger β range[34] to realize an ultralow-power saturable or reverse saturable absorber for applications in ultrafast lasing, optical limiters and on–off all-optical switching.

The nonlinear dynamics of the overall system are primarily dictated by the nonlinear response of the ITO film[1]. A positive change

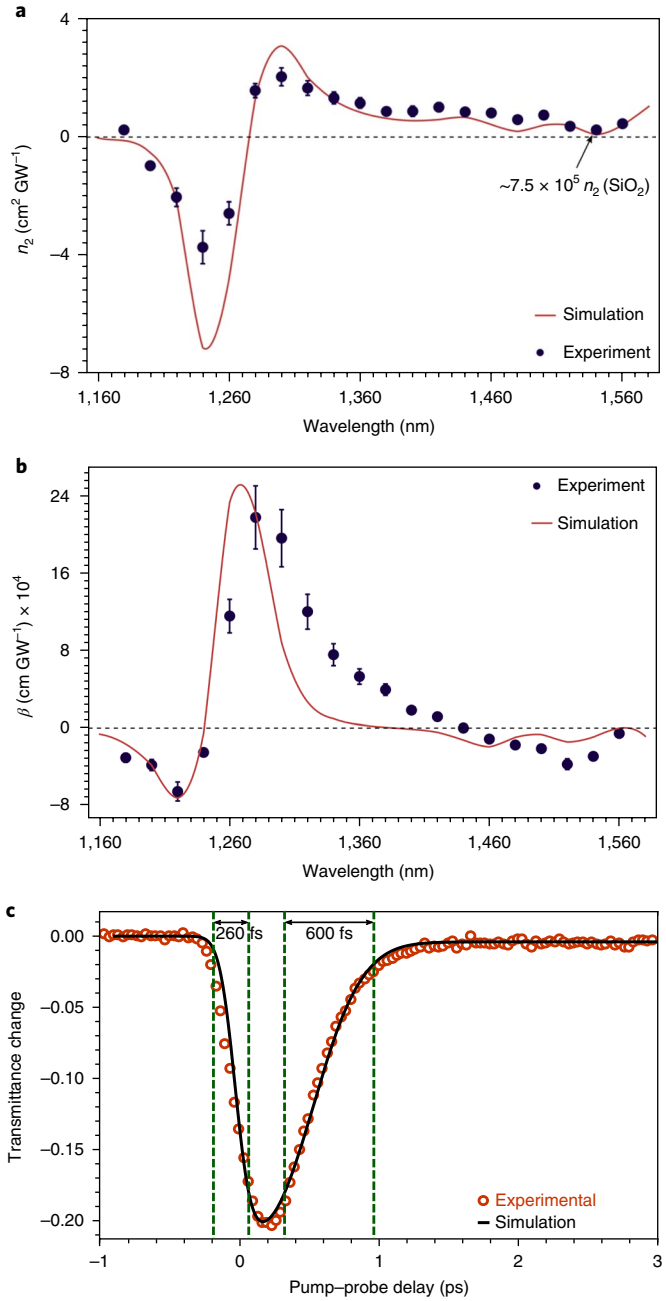

Fig. 2 | Nonlinear response of the coupled system. a, Effective nonlinear refractive index n_2, measured using a *Z*-scan technique. The metasurface exhibits a large nonlinear response. The intensity-dependent refractive index of the metasurface is almost six orders of magnitude larger than that of SiO_2, even for a highly red-detuned wavelength ($\lambda = 1{,}540$ nm). **b**, Nonlinear absorption β. Solid lines show the simulated n_2 and β values, calculated using a two-temperature model while taking the non-parabolic conduction band structure of the ITO into consideration (see Supplementary Section 'Electronic dispersion relation in ITO'). The semi-quantitative numerical simulation predicts the main features of the wavelength-dependent nonlinear response. Error bars correspond to the uncertainity in measured values due to distortion of the *Z*-scan traces. **c**, Pump-induced change in the transmittance of the probe at 1,280 nm. Dashed vertical lines represent the 10–90% transient time. The slow recovery time is dictated by the electron–phonon coupling strength and the quality factor of the resonance of the coupled system.

in the refractive index of ITO—resulting from an ultrafast redshift of the plasma frequency—leads to a redshift of the main resonance of the coupled system due to the change in the coupling conditions between the antenna and the bulk plasmon mode of the ITO. A laser pulse at a red-detuned (blue-detuned) wavelength thus experiences an increase (decrease) in effective refractive index, that is, a positive (negative) value of the intensity-dependent refractive index. Thus, by choosing appropriate geometric parameters of the antenna array and the zero-permittivity wavelength of the ENZ film, one can control the sign of the nonlinearity.

We studied the temporal dynamics of the resonant nonlinear response using a degenerate pump–probe transmittance measurement at $\lambda = 1{,}280$ nm. The measurement (Fig. 2c) revealed a rise time of ~260 fs and recovery time of ~600 fs. The rise-time measurement was constrained by the temporal width of the pump pulse, suggesting an onset of nonlinearity with sub-100 fs dynamics. The total response time (the rise time plus the recovery time) at the resonant wavelength is only 53% larger than that of the bare ITO film (see Supplementary Information Fig. 10). The relatively slower response time can be attributed to the resonance effect of the coupled structure. The nonlinear response of the coupled structure can be further improved by using nanoantennas with higher quality factor *Q*, but possibly at the expense of a slower response time[35].

Finally, we investigated the nonlinear contribution to the refractive index at higher intensities by measuring the nonlinear phase shift $\Delta\phi$ as a function of intensity at four different wavelengths (Fig. 3), two tuned to the main resonance ($\lambda = 1{,}250$ nm and $\lambda = 1{,}265$ nm) and two red-detuned from the main resonance ($\lambda = 1{,}360$ nm and $\lambda = 1{,}440$ nm). The maximum resonant nonlinear phase shift was $\Delta\phi = 0.677$ rad, which can occur due to a refractive index change of approximately −2.74 for propagation through a 50-nm-thick material. Even at $\lambda = 1{,}440$ nm (a highly red-detuned wavelength), the change to the refractive index is ~2.6, while the change in the transmittance is less than 6%. Such a broadband, large and ultrafast optically induced change in the refractive index is unprecedented. In most cases, saturation effects become evident for an incident energy density larger than ~2 pJ μm^{-2}, which is lower than the damage threshold of the gold antennas. The saturation of Δn can be attributed to various causes, including large damping of the low-conductivity ITO, which limits the maximum achievable temperature of the free electrons. Furthermore, the increased electron temperature spectrally widens the resonance of the coupled structure, limiting the maximum phase shift achievable. Thus, ENZ materials with lower intrinsic damping could increase the saturation threshold. The nonlinear response could be further enhanced by maximizing the overlap between the near-field of the antennas and the ITO layer, by choosing antennas (dielectric or metallic) with higher quality factors, and by choosing an ENZ material with lower intrinsic damping[18,36].

We note that when the ENZ medium is sufficiently thick, the antenna resonance becomes locked to the zero permittivity wavelength of the ENZ material[37]. Nevertheless, a metasurface that incorporates a thick ENZ material will also exhibit an enhanced nonlinear response because a dynamic change in the substrate's refractive index necessarily modifies the resonance wavelength of the antenna. The strategy introduced in this Letter can be considered as a temporal analogue of the typical space-gradient metasurface[22–25,27]. Thus, by combining both strategies one could design an all-optical space–time gradient metasurface to break the geometrical and temporal symmetry on-chip[38,39], design ultrafast temporal holograms and control the directivity of emission using an optical gate signal[40,41].

In summary, we have demonstrated that a metasurface geometry is uniquely suited to achieving large nonlinear refraction. We have shown that a metasurface may exhibit an extremely large intensity-dependent refractive index if an ENZ medium is incorporated into the design. The technique introduced in this Letter offers flexibility in customizing both the wavelength-dependent

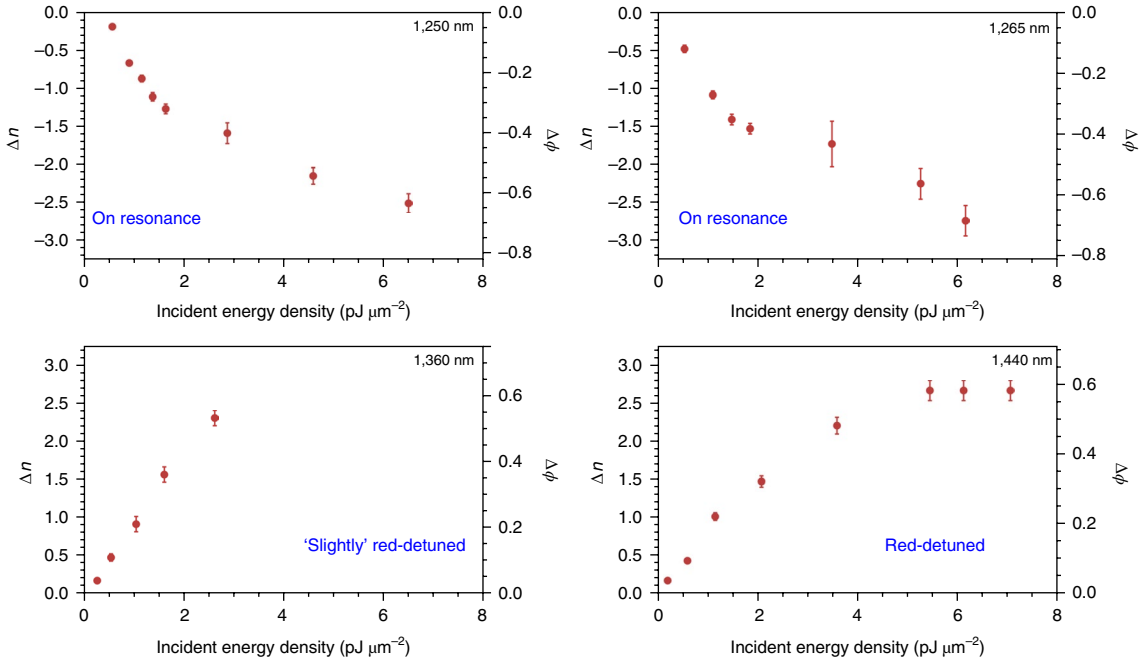

Fig. 3 | Maximum nonlinear contribution to the refractive index as a function of incident energy density. We determined the maximum nonlinear contribution to the refractive index by measuring the phase shifts at four different wavelengths for a series of different incident energy densities. Even at a highly red-detuned wavelength of 1,440 nm, the maximum nonlinear contribution to the refractive index is larger than 2.5. These results show that the metasurface exhibits a large refractive index change across a wide bandwidth. We note that the saturation effects present in the plots can be modelled to extract the effective fifth-order nonlinear coefficients. The error bars correspond to the uncertainty in measured values due to the distortion of the *Z*-scan traces.

magnitude and the signs of the nonlinear refractive index and the nonlinear absorption coefficient in any optical frequency of interest. The 50-nm-thick proof-of-concept metasurface exhibits a large broadband nonlinear response with sub-picosecond recovery time. The maximum absolute value of the nonlinear refractive index of the metasurface is three orders of magnitude larger than the bare, planar ITO at normal incidence[1]. As a benchmark comparison, it is also seven orders of magnitude larger than that of glass and four orders of magnitude larger than those of GaAs and As_2S_3 (ref. [42]). However, the large absorption in the coupled structure is a constraint. From the operational point of view, perhaps a more important criterion is the maximum achievable nonlinear phase shift over one absorption length. The maximum theoretical absorption in the structure (including the ohmic loss in metal) over the entire spectral range of interest is less than 40% (see Supplementary Section 'Field enhancement and absorption'). Further improvements to the design and material selection, such as dielectric nanoantennas and an ENZ material with less damping, may reduce the overall absorption while increasing the efficiency. More interestingly, the magnitude of the maximum nonlinear contribution to the refractive index (>2.5) is comparable to or larger than the linear refractive index of typical optical materials. Our findings introduce a new paradigm for developing efficient nonlinear media for applications involving low-power, high-integration-density nonlinear nanophotonic devices, and also demonstrate a subwavelength nonlinear metasurface for ultrafast all-optical control of the phase, amplitude and polarization of light.

Methods

Methods, including statements of data availability and any associated accession codes and references, are available at https://doi.org/10.1038/s41566-017-0089-9.

Received: 22 May 2017; Accepted: 20 December 2017;
Published online: 26 January 2018

References

1. Alam, M. Z., De Leon, I. & Boyd, R. W. Large optical nonlinearity of indium tin oxide in its epsilon-near-zero region. *Science* **352**, 795–797 (2016).
2. Miller, D. A. B. Are optical transistors the logical next step? *Nat. Photon.* **4**, 3–5 (2010).
3. Sherwood-Droz, N. et al. Optical 4×4 hitless silicon router for optical networks-on-chip (NoC). *Opt. Express* **16**, 15915–15922 (2008).
4. Boyd, R. W., Gehr, R. J., Fischer, G. L. & SipeJ. Nonlinear optical properties of nanocomposite materials. *J. Eur. Opt. Soc. A* **5**, 505–512 (1996).
5. Boyd, R. W. & Sipe, J. E. Nonlinear optical susceptibilities of layered composite materials. *J. Opt. Soc. Am. B* **11**, 297–303 (1994).
6. Sarychev, A. K. & Shalaev, V. M. Electromagnetic field fluctuations and optical nonlinearities in metal-dielectric composites. *Phys. Rep.* **335**, 275–371 (2000).
7. Abb, M., Albella, P., Aizpurua, J. & Muskens, O. L. All-optical control of a single plasmonic nanoantenna–ITO hybrid. *Nano Lett.* **11**, 2457–2463 (2011).
8. Abb, M., Wang, Y., de Groot, C. H. & Muskens, O. L. Hotspot-mediated ultrafast nonlinear control of multifrequency plasmonic nanoantennas. *Nat. Commun.* **5**, 4869 (2014).
9. Lee, J. et al. Giant nonlinear response from plasmonic metasurfaces coupled to intersubband transitions. *Nature* **511**, 65–69 (2014).
10. Yang, Y. et al. Nonlinear Fano-resonant dielectric metasurfaces. *Nano Lett.* **15**, 7388–7393 (2015).
11. Minovich, A. E. et al. Functional and nonlinear optical metasurfaces. *Laser Photon-. Rev.* **9**, 195–213 (2015).
12. Ren, M. et al. Nanostructured plasmonic medium for terahertz bandwidth all-optical switching. *Adv. Mater.* **23**, 5540–5544 (2011).
13. Liberal, I., Mahmoud, A. M., Li, Y., Edwards, B. & Engheta, N. Photonic doping of epsilon-near-zero media. *Science* **355**, 1058–1062 (2017).
14. Engheta, N. Pursuing near-zero response. *Science* **340**, 286–287 (2013).
15. Edwards, B., Alù, A., Young, M. E., Silveirinha, M. & Engheta, N. Experimental verification of epsilon-near-zero metamaterial coupling and energy squeezing using a microwave waveguide. *Phys. Rev. Lett.* **100**, 033903 (2008).
16. Alù, A., Silveirinha, M. G., Salandrino, A. & Engheta, N. Epsilon-near-zero metamaterials and electromagnetic sources: tailoring the radiation phase pattern. *Phys. Rev. B* **75**, 155410 (2007).
17. Silveirinha, M. & Engheta, N. Tunneling of electromagnetic energy through subwavelength channels and bends using ε-near-zero materials. *Phys. Rev. Lett.* **97**, 157403 (2006).

18. Caspani, L. et al. Enhanced nonlinear refractive index in ϵ-near-zero materials. *Phys. Rev. Lett.* **116**, 233901 (2016).
19. Neira, A. D. et al. Eliminating material constraints for nonlinearity with plasmonic metamaterials. *Nat. Commun.* **6**, 7757 (2015).
20. Capretti, A., Wang, Y., Engheta, N. & Dal Negro, L. Enhanced third-harmonic generation in Si-compatible epsilon-near-zero indium tin oxide nanolayers. *Opt. Lett.* **40**, 1500–1503 (2015).
21. Luk, T. S. et al. Enhanced third harmonic generation from the epsilon-near-zero modes of ultrathin films. *Appl. Phys. Lett.* **106**, 151103 (2015).
22. Yu, N. et al. Light propagation with phase discontinuities: generalized laws of reflection and refraction. *Science* **334**, 333–337 (2011).
23. Ni, X., Emani, N. K. Kildishev, A. V., Boltasseva, A. & Shalaev, V. M. Broadband light bending with plasmonic nanoantennas. *Science* **335**, 1214686 (2012).
24. Kildishev, A. V., Boltasseva, A. & Shalaev, V. M. Planar photonics with metasurfaces. *Science* **339**, 1232009 (2013).
25. Yu, N. & Capasso, F. Flat optics with designer metasurfaces. *Nat. Mater.* **13**, 139–150 (2014).
26. High, A. A. et al. Visible-frequency hyperbolic metasurface. *Nature* **522**, 192–196 (2015).
27. Lin, D., Fan, P., Hasman, E. & Brongersma, M. L. Dielectric gradient metasurface optical elements. *Science* **345**, 298–302 (2014).
28. Chong, K. E. et al. Polarization-independent silicon metadevices for efficient optical wavefront control. *Nano Lett.* **15**, 5369–5374 (2015).
29. Vassant, S. et al. Epsilon-near-zero mode for active optoelectronic devices. *Phys. Rev. Lett.* **109**, 237401 (2012).
30. Campione, S., Brener, I. & Marquier, F. Theory of epsilon-near-zero modes in ultrathin films. *Phys. Rev. B* **91**, 121408 (2015).
31. Campione, S., Wendt, J. R., Keeler, G. A. & Luk, T. S. Near-infrared strong coupling between metamaterials and epsilon-near-zero modes in degenerately doped semiconductor nanolayers. *ACS Photon-.* **3**, 293–297 (2016).
32. Schulz, S. A. et al. Optical response of dipole antennas on an epsilon-near-zero substrate. *Phys. Rev. A* **93**, 063846 (2016).
33. Sheik-Bahae, M., Said, A. A., Wei, T.-H., Hagan, D. J. & Van Stryland, E. W. Sensitive measurement of optical nonlinearities using a single beam. *IEEE J. Quantum Electron.* **26**, 760–769 (1990).
34. Luk, T. S. et al. Directional perfect absorption using deep subwavelength low-permittivity films. *Phys. Rev. B* **90**, 085411 (2014).
35. Khurgin, J. B., Sun, G., Chen, W. T., Tsai, W.-Y. & Tsai, D. P. Ultrafast thermal nonlinearity. *Sci. Rep.* **5**, 17899, https://doi.org/10.1038/srep17899 (2015).
36. Sachet, E. et al. Dysprosium-doped cadmium oxide as a gateway material for mid-infrared plasmonics. *Nat. Mater.* **14**, 414–420 (2015).
37. Kim, J. et al. Role of epsilon-near-zero substrates in the optical response of plasmonic antennas. *Optica* **3**, 339–346 (2016).
38. Hadad, Y., Sounas, D. & Alu, A. Space–time gradient metasurfaces. *Phys. Rev. B* **92**, 100304 (2015).
39. Yu, Z. & Fan, S. Complete optical isolation created by indirect interband photonic transitions. *Nat. Photon-.* **3**, 91–94 (2009).
40. Staude, I. et al. Tailoring directional scattering through magnetic and electric resonances in subwavelength silicon nanodisks. *ACS Nano* **7**, 7824–7832 (2013).
41. Kuznetsov, A. I., Miroshnichenko, A. E., Brongersma, M. L., Kivshar, Y. S. & Luk'yanchuk, B. Optically resonant dielectric nanostructures. *Science* **354**, aag2472 (2016).
42. Boyd, R. W. *Nonlinear Optics* (Academic Press, Cambridge, MA, 2003).
43. Campione, S., Kim, I., de Ceglia, D., Keeler, G. A. & Luk, T. S. Experimental verification of epsilon-near-zero plasmon polariton modes in degenerately doped semiconductor nanolayers. *Opt. Express* **24**, 18782–18789 (2016).
44. Liu, X. et al. Quantification and impact of nonparabolicity of the conduction band of indium tin oxide on its plasmonic properties. *Appl. Phys. Lett.* **105**, 181117 (2014).
45. Kane, E. O. Band structure of indium antimonide. *J. Phys. Chem. Solids* **1**, 249–261 (1957).

Acknowledgements

The authors acknowledge support from the Canada Excellence Research Chairs Program, the Natural Sciences and Engineering Research Council of Canada (NSERC), and the Canada Foundation for Innovation (CFI). I.D.L. acknowledges financial support from CONACyT (Ciencia Básica) grant no. 286150. M.Z.A. thanks S. Choudhary for discussions on the linewidth broadening mechanisms in a plasmonic system.

Author contributions

I.D.L. conceived the idea and initiated the study. I.D.L., S.A.S., M.Z.A. and J.U. designed the sample. S.A.S. performed the FDTD simulations. S.A.S. and J.U. fabricated the sample. M.Z.A. performed all experiments and the corresponding data analysis, developed the numerical model to describe the nonlinear response, and wrote the first draft. All authors contributed to finalizing the manuscript. I.D.L. and R.W.B. supervised the project.

Competing interests

R.W.B. is the co-founder and Chief Technology Officer of KBN Optics, Pittsford NY.

Additional information

Supplementary information is available for this paper at https://doi.org/10.1038/s41566-017-0089-9.

Reprints and permissions information is available at www.nature.com/reprints.

Correspondence and requests for materials should be addressed to I.D.

Publisher's note: Springer Nature remains neutral with regard to jurisdictional claims in published maps and institutional affiliations.

Methods

Design. We used a commercial finite-difference time-domain (FDTD) software (Lumerical FDTD solutions) to design the metasurface. The material dispersion was taken into account by using experimental values for the permittivity of ITO. The permittivity of the ITO film was measured using a spectroscopic ellipsometer. The antenna was designed by choosing the length-to-width ratio in such a way so that the fundamental dipole resonance of the antenna in the absence of the ITO film (that is, assuming only the glass substrate) lies near the zero crossing wavelength of the permittivity of the ITO film. The fabricated antennas had average dimensions of ~370 nm × 110 nm × 27 nm (the designed dimension was ~355 nm × 110 nm × 27 nm) and the unit cell dimension was 600 nm × 600 nm. The ITO film was 23 nm thick with a surface resistivity of ~80 $\Omega\square^{-1}$.

Fabrication. The 500 μm × 500 μm antenna array was fabricated on commercially available ITO on glass substrates (PGO GmbH). The antenna patterns were defined in a bilayer poly(methylmethacrylate) resist using electron beam lithography (Raith Pioneer 30 kV), followed by Au deposition and a liftoff step. Intraparticle proximity error correction was used to ensure sharp corners and a good rectangular shape of the antennas[46].

Measurements. The linear response of the metasurface was measured using a thermal light source and a custom-built transmittance measurement system. We used a single-beam *Z*-scan technique to measure the nonlinear response of the system using a regeneratively amplified femtosecond laser pumped optical parametric amplifier as the source laser. The pulse width was ~140 fs. A pair of apertures was used to produce a beam with a circularly symmetric trimmed Airy profile (that is, only the central lobe of an Airy pattern) in the far-field. A pair of achromatic doublet lenses was then used to collimate and enlarge the beam. Part of the collimated beam was routed to a reference photodiode to monitor power fluctuations. The rest of the collimated beam was focused onto the sample using an achromatic doublet lens with antireflection coating. The diffracted light after the sample was split using a pellicle beamsplitter, and routed to a pair of detectors for closed- and open-aperture measurements. The sample was mounted on a computer-controlled motorized translation stage. For each position of the sample we recorded truncated mean values (the lowest 25% and highest 25% values were discarded before calculating the mean) from the photodiodes averaged over ~3,000 pulses. Due to the diffractive propagation required to produce a collimated beam with an Airy profile, the beam diameter at the *Z*-scan lens varied as a function of wavelength. Specifically, the input beam diameter varied from 10.2 ± 0.15 mm to 14.65 ± 0.15 mm for $\lambda = 1{,}160$ nm to $\lambda = 1{,}560$ nm. The beam was focused onto the sample using an antireflection-coated achromatic doublet lens of ~100 mm focal length. The closed-aperture detector was placed 285 mm away from the *Z*-scan lens. We did not use any aperture before the closed-aperture detector because the active area (5 mm diameter) of the detector was much smaller than the beam diameter. The use of an even smaller aperture adversely affected the measurement by reducing the signal-to-noise ratio.

We used the Fresnel–Kirchhoff diffraction integral with a fast-Fourier-transform-based beam propagation method to simulate the experimental beam propagation over the entire set-up. We were thus able to calculate the *z*-dependence of the light falling onto the closed- and open-aperture photodiodes. We wrote the numerical beam propagation program using Julia language[47], which allows arbitrary order nonlinear refraction and absorption to be taken into account. We have observed that at high intensity fifth-order nonlinear absorption becomes significant, and at non-resonant wavelengths it can almost completely cancel the third-order nonlinear absorption.

Numerical model of the nonlinear refractive index. To calculate the nonlinear refractive index, we carried out a series of linear FDTD simulations of the antenna–ITO structure by varying the plasma frequency of the ITO. We then calculated the homogenized refractive index from each set of *s*-parameters, resulting in a plasma frequency-dependent effective index distribution of the coupled system. We then calculated the time-dependent electronic temperature using a semiclassical two-temperature model. The plasma frequency of the ITO layer was calculated based on the electronic temperature (see Supplementary Section 'Two-temperature model'). Based on the calculated plasma frequency and the set of homogenized refractive indices, we calculated the time-dependent change in the refractive index. The effective nonlinear coefficients n_2 and β were determined by dividing the time-averaged homogenized refractive index (normalized by the pulse shape) by the incident intensity. In this model, we ignore the intrinsic nonlinearity of the metal and the change in absorption of the coupled system due to the temperature-dependent change in the damping coefficient (imaginary part of the permittivity) of the ITO layer. This leads to an overestimation of β obtained from the numerical model for all wavelengths far from the saturation intensity. Hence, we scaled down the β values by a factor of 3.0 to fit the numerical result to that obtained in the experiment.

Code availability. All relevant code used in this paper are available from the corresponding author upon reasonable request.

Data availability. All relevant data used in this paper are available from the corresponding author upon reasonable request.

References

46. Schulz, S. A. et al. Quantifying the impact of proximity error correction on plasmonic metasurfaces [invited]. *Opt. Mater. Express* **5**, 2798–2803 (2015).
47. Bezanson, J., Edelman, A., Karpinski, S. & Shah, V. B. Julia: a fresh approach to numerical computing. *SIAM Rev.* **59**, 65–98 (2017).

nature photonics

SUPPLEMENTARY INFORMATION

https://doi.org/10.1038/s41566-017-0089-9

In the format provided by the authors and unedited.

Large optical nonlinearity of nanoantennas coupled to an epsilon-near-zero material

M. Zahirul Alam[1], Sebastian A. Schulz[1,2,3], Jeremy Upham[1], Israel De Leon[4*] and Robert W. Boyd[1,5]

[1]Department of Physics, University of Ottawa, Ottawa, ON, Canada. [2]Centre for Advanced Photonics and Process Analysis, Cork Institute of Technology, Cork, Ireland. [3]Tyndall National Institute, Cork, Ireland. [4]School of Engineering and Sciences, Tecnologico de Monterrey, Monterrey, NL, Mexico. [5]Institute of Optics and Department of Physics and Astronomy, University of Rochester, Rochester, NY, USA. *e-mail: ideleon@itesm.mx

Linear response of ITO

We measured the permittivity of the 23 nm ITO using ellipsometry (Fig.S1). For the entire spectral range the following Drude-Loretz model can quantify the permittivity:

$$\varepsilon = \varepsilon_\infty + \frac{(\varepsilon_s - \varepsilon_\infty)\omega_t^2}{\omega_t^2 - \omega^2 - i\Gamma_0\omega} - \frac{\omega_p^2}{\omega^2 + i\Gamma_d\omega}. \tag{1}$$

We use the following values for the parameters. $\varepsilon_\infty = 3.1178$, $\varepsilon_s = 3.8466980$, $\omega_t = 7.42969 \times 10^{15}$ rad/sec, $\omega_p = 2.6594 \times 10^{15}$ rad/sec, $\Gamma_0 = 0.534217 \times 10^{15}$ rad/sec, $\Gamma_d = 0.231806 \times 10^{15}$ rad/sec.

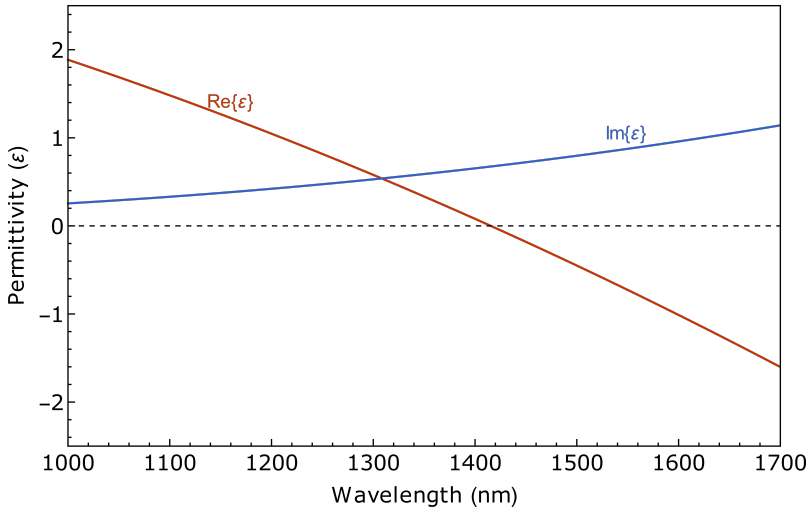

Figure S1. Permittivity of ITO: The real part of permittivity of the low conductivity ITO crosses zero at 1420 nm.

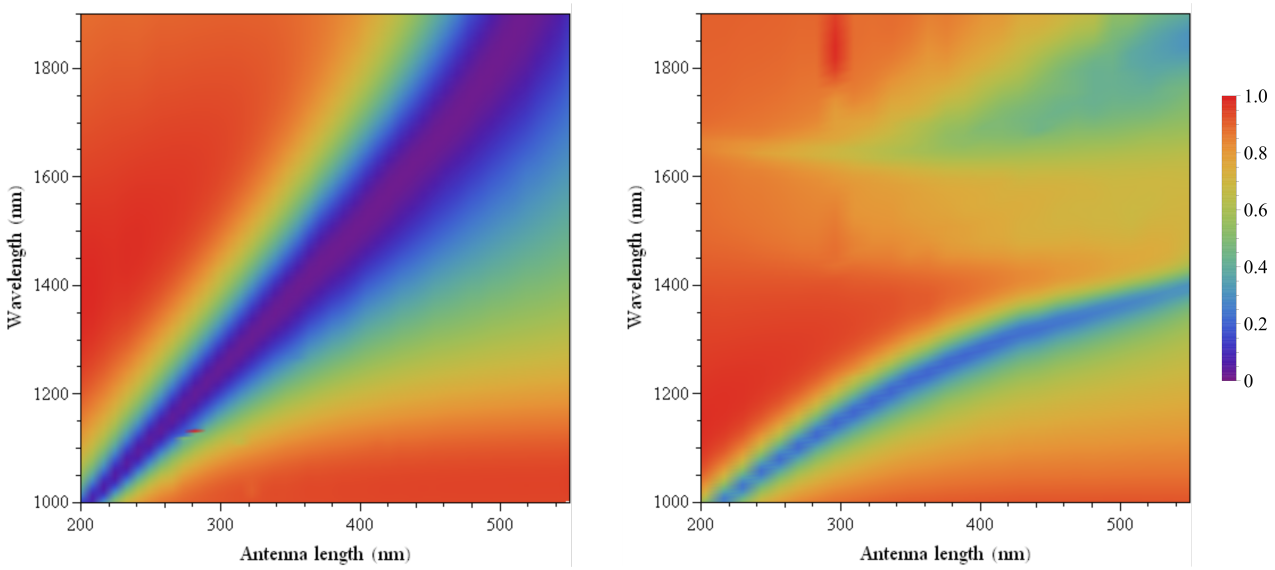

Figure S2. Strong coupling: Length dependent variation in the transmittance of gold dipole antenna on glass in the absence of an ITO layer (left panel) and with an ITO layer between the antenna and the substrate (right panel).

Linear response of the coupled system

A thin ENZ layer supports a bulk plasma mode with wavevector-dependent radiative and nonradiative properties at the zero permittivity wavelength. This mode has been theoratically and experimentally investigated in a number of papers.[1,2] When a

dipole antenna with resonance near the bulk plasma mode is placed on the ITO layer, the antenna mode and the bulk plasma mode interacts. This interaction results in strong coupling induced splitting of the antenna resonance. Fig. S2 shows an anti-crossing in the coupled structure which is a signature that antenna-ITO is in strong coupling regime. This artificial polariton splitting ($\sim \lambda/4$) is one of the largest observed in metamaterials.[3–5] The shape and the magnitude of the resonance dips of the ITO-antenna coupled structure depend on the coupling strength and the material parameters. The spectral width of the resonance of the coupled system at the shorter wavelength is narrower than that of antenna only.

Electronic dispersion relation in ITO

ITO has a non-parabolic conduction band.[6] Following Kane's model[7,8] of semiconductor we can write the energy-wavevector (E, k) dispersion relation for a conduction band electron of ITO as

$$\frac{\hbar^2 k^2}{2m} = E + CE^2, \tag{2}$$

where $C = 0.4191$ eV^{-1} is the non-parabolicity parameter and we have used the value reported by Liu et. al.[6] $m = 0.4m_e$ is the effective mass of the electrons. From the above relation we find

$$k = \sqrt{2mE(1+CE)/\hbar^2}, \tag{3}$$

$$dk = \sqrt{\frac{2m}{\hbar^2}}\frac{1+2CE}{2\sqrt{E+CE^2}}dE. \tag{4}$$

The number of states available for a given magnitude of wavevector $|k|$ can be found by constructing a spherical shell of radius $|k|$ and thickness dk. The volume of this spherical shell in the momentum space is $4\pi k^2 dk$. The number of k states within the spherical shell, $g(k)dk$, is

$$g(k)dk = \frac{1}{2^3} \times 2 \times 4\pi k^2 \frac{V}{\pi^3} dk. \tag{5}$$

The factor 2 is the spin degeneracy factor of electrons. The factor $1/2^3$ is to avoid counting indistinguishable wavefunctions differing in signs only. Now by using Eqns. (3) and (4) and by dividing by the volume V, we can find the density of states $g(E)$, defined as the number of electron states in the conduction band per unit volume over an energy range dE,

$$g(E) = \frac{\sqrt{2}}{\pi^2}\left(\frac{m}{\hbar^2}\right)^{\frac{3}{2}} [(1+CE)]^{\frac{1}{2}} (1+2CE) \tag{6}$$

The total number of electrons n can be found by integrating the product of the Fermi-Dirac distribution function (f_{FD}) and the density of states over all energy range

$$n = \int_0^\infty f_{FD}(E, \mu(T_e), T_e) g(E) dE, \tag{7}$$

where $\mu(T_e)$ is the electro-chemical potential which depends on the electron temperature T_e due to the conservation of total electron number in the conduction band. Thus, the electron number conservation requirement results in decreasing value of the chemical potential with increasing electron temperature.

We can write the plasma frequency as[9,10]

$$\omega_p^2(T_e) = \frac{e^2}{3m\varepsilon_0\pi^2} \int_0^\infty dE(1+2CE)^{-1} \left(\frac{2m}{\hbar^2}(E+CE^2)\right)^{\frac{3}{2}} \left(-\frac{\partial f_{FD}(E, \mu(T_e), T_e)}{\partial E}\right). \tag{8}$$

The expression $\left(-\frac{\partial f_{FD}}{\partial E}\right)$ is a measure of the strength of the thermal broadening of the electronic distribution around the Fermi level. For electrons in a room temperature solid the thermal broadening function is narrow and is zero beyond a few $k_B T$ from the Fermi level. However, an elevated electron temperature leads to the broadening of this function due to a strong modification of the Fermi-Dirac distribution. The modification of the Fermi-Dirac distribution is much stronger in ITO than a noble metal due to the lower heat capacity constant of the free electrons of ITO. This results in an electron-temperature-dependent plasma frequency of ITO due to the temperature dependence of the electro-chemical potential (the effective mass of the electrons) as required by Eq.(7). For a given electronic temperature we find the chemical potential from Eqn. (7), and use Eqn. (8) to find the plasma frequency of ITO which we insert into the Drude-Lorentz model of ITO to calculate the permittivity of ITO at an elevated electron temperature. For a parabolic band ($C = 0$) the above expression reduces to the well known expression of the plasma frequency.[10]

Two-temperature model

The free-electron dynamics in ITO are metal-like and can be described by the Drude model. The third-order self-focusing nonlinearity of ITO in the ENZ regime is dominated by the response of the free-electrons. To describe this nonlinear mechanism, we use a phenomenological two-temperature model.[11–13] The nonlinear process due to the hot-electron dynamics has a finite response time and the maximum response is delayed with respect to the peak of the laser excitation. In noble metals the total relaxation time of the hot electrons is a few picoseconds and is limited by the electron-phonon interaction time. However the response of the ITO thin film deviates from that of the metal in three important ways: i) unlike noble metals, ITO has no interband transition resonance in the visible or infrared range of the optical spectrum; ii) the free-electron density in ITO is almost two orders of magnitude smaller than that of noble metals such as gold, resulting in much smaller electron heat capacity and larger change in the electron temperature if all other parameters are held constant; and iii) owing to a relatively smaller free-electron density, the Fermi level is quite low in the conduction band (~ 1 eV for ITO). Due to the last property, infrared radiation at ENZ wavelengths can excite even the lowest-energy conduction band electrons (in contrast, the Fermi level of gold is ~ 6.42 eV and IR light only excite only those electrons that sit near the Fermi level).

According to the delayed two-temperature model, after the laser pulse is absorbed, the generated hot electrons acquire a non-thermal energy distribution and act as a delayed source of energy. The overall dynamics of the conduction band electrons can be described by the following system of phenomenological coupled differential equations:[13]

$$\begin{aligned} C_e\frac{\partial T_e(t)}{\partial t} &= -g_{ep}(T_e(t)-T_l(t))+\frac{N_{th}(t)}{2\tau_{ee}(t)}, \\ C_l\frac{\partial T_l}{\partial t} &= g_{ep}(T_e(t)-T_l(t))+\frac{N_{th}}{\tau_{ep}(t)}, \\ \frac{\partial N(t)}{\partial t} &= -\frac{N(t)}{2\tau_{ee}(t)}-\frac{N(t)}{\tau_{ep}(t)}+P, \end{aligned} \tag{9}$$

Here, N is the non-thermal energy density stored in the excited electrons, g_{ep} is the electron-phonon coupling coefficient, T_e (T_l) is the free-electron (lattice) temperature, C_e (C_l) is the heat capacity of the electrons (lattice), τ_{ee} (τ_{ep}) is the electron-electron (electron-phonon) relaxation time, and P is the time dependent absorbed power density (i.e., rate of energy density absorbed in the material). We have ignored thermal diffusion processes in Eq. (9). In the transverse dimension the beam size greatly exceeds the electrons thermal diffusion length and hence we also ignore the transverse dependence. We have also ignored the thermal diffusion in the longitudinal direction by assuming constant absorbed energy density due to small thickness of the ITO film.

Next we estimate the different parameters for ITO that appear in Eq. (9). We calculate the electron heat capacity C_e by using[14]

$$C_e(T_e)=\int Eg(E)\frac{\partial f_{FD}(\mu(T_e),T_e)}{\partial T_e}dE \tag{10}$$

We take the lattice heat capacity $C_l = 2.54\times10^6$ Jm^{-3}K to be a constant due to relatively small change in the lattice temperature.[15]

The electron-electron scattering rate ($\Gamma_{ee}=1/\tau_{ee}$) determines the time duration electrons require to reach to thermal equilibrium with each other. We use the following relation to estimate the temperature dependent electron-electron scattering rate[16]

$$\Gamma_{ee}=\frac{\omega^2}{4\pi^2\omega_p(T_e)}\left[1+\left(\frac{2\pi k_B T_e}{\hbar\omega}\right)^2\right] \tag{11}$$

The electron-phonon scattering rate (Γ_{eph}) depends on the lattice temperature and the Debye temperature of the lattice ($\Theta_D = 900K$)

$$\Gamma_{eph}=\Gamma_0\left[\frac{2}{5}+\frac{4T_L^5}{\Theta_D^5}\int_0^{\theta_D/T_l}\frac{z^4}{e^z-1}dz\right]. \tag{12}$$

The electron-phonon coupling coefficient (g_{ep}) determines the rate of the energy exchange between the excited hot electrons and the vibrational modes of the lattice. Due to the strong modification of the conduction band electron distribution, even the electrons with initial energy much below the Fermi level take part in this energy exchange process. Hence we estimate the electron-phonon coupling coefficient using a relation which includes the density of states of the conduction band[14]

$$g_{ep}=\frac{\pi k_B}{\hbar g(E_F)}\lambda_{ep}<(\hbar\omega_{ph})^2>\int g^2(E)\frac{-\partial f_{FD}}{\partial E}dE, \tag{13}$$

where λ_{ep} is the electron-phonon mass enhancement parameter and the second moment of phonon spectrum $< (\hbar\omega_{ph})^2 >$ is an empirical parameter. We take $\lambda_{ep} < (\hbar\omega_{ph})^2 >= 0.0042\ eV^2$ are a few times smaller than nobel metals such as gold.[14]

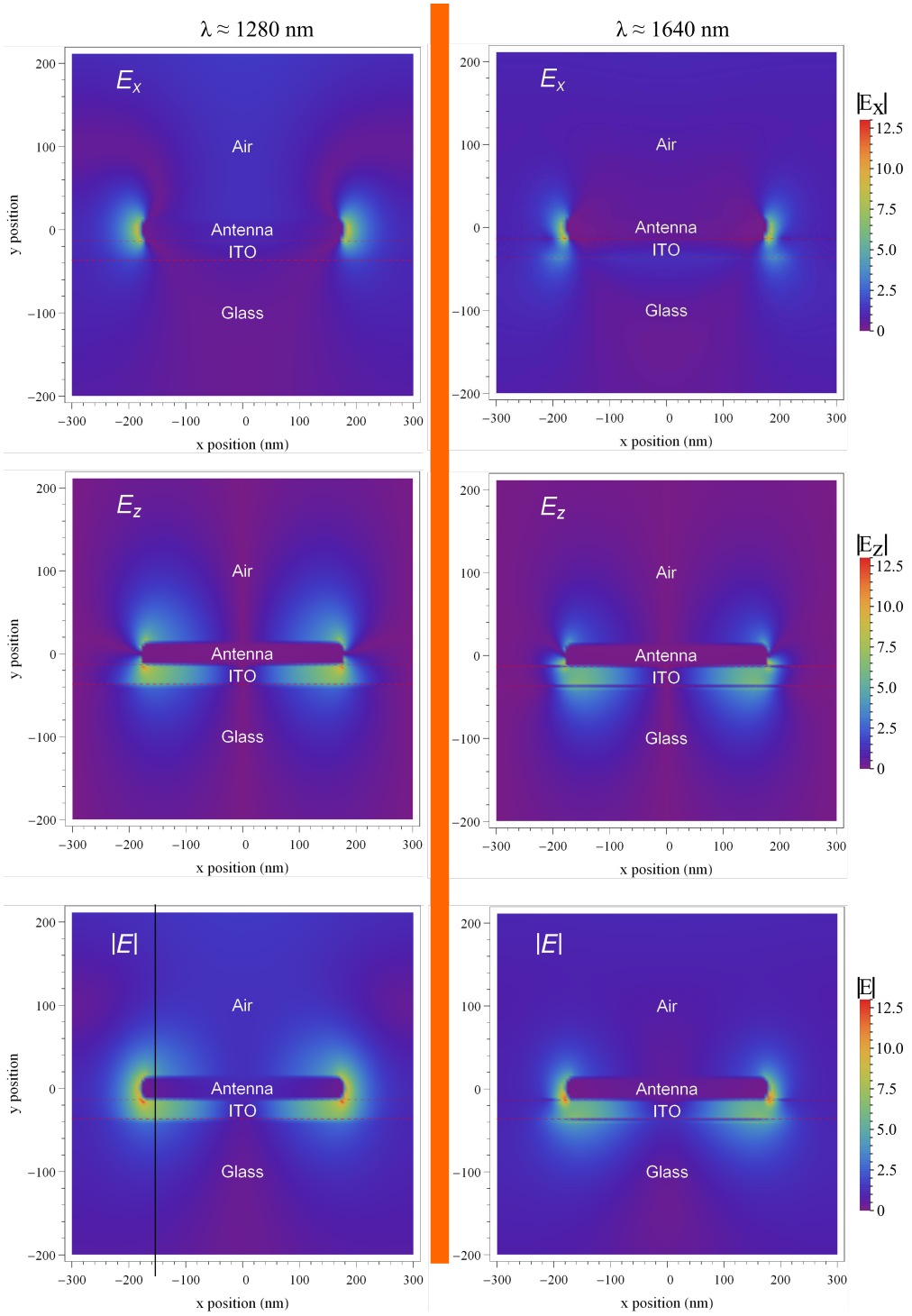

Figure S3. Field distribution: The plots show the field distribution at two resonances ($\lambda \approx 1280$ nm and $\lambda \approx 1640$ nm). The left panel shows the field distribution of the resonance at the short wavelength (the resonace of interest for this report). The right panel shows the field distribution at the resonance located at the long wavelength (we have not investigated the response at this wavelength). The z-components of the electric field profile shows the main difference between the two modes of the coupled structure. The edges of the antennas are rounded with a rounding radius of 7 nm. We plot the wavelength-dependent intensity enhancement along the vertical black line in the next figure.

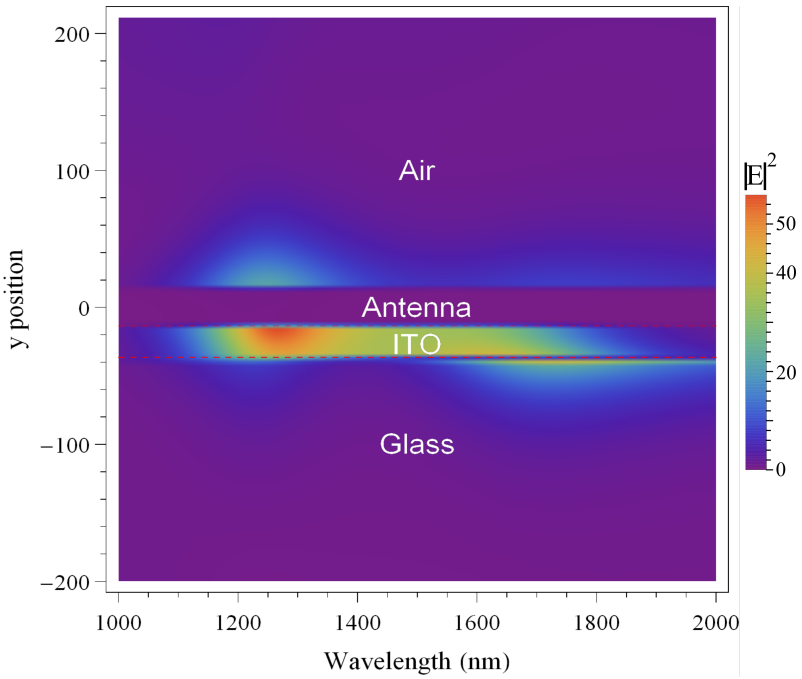

Figure S4. Wavelength-dependent intensity enhancement: Shown inside the ITO layer of the coupled structure, for a fixed x-position – along the vertical black line in Fig. S3 – when excited from air.

Field enhancement and absorption

The antennas placed on the ITO film allow electric field to be concentrated inside the ITO structure resulting in enhancement of the field intensity. Figure S4 shows the calculated intensity enhancement factor, as a function of position and wavelength, sufficiently far from the antenna edge to avoid hotspots. The fabricated dipole antennas differ from the simulated ones due to the fabrication imperfection which results in antenna edges being rounded off. We took this into account in the simulation by rounding the edges (7 nm rounding radius) of the antennas. Furthermore, in our calculation of the two-temperature model we take the calculated intensity enhancement (averaged over the ITO thickness) by considering the electric field enhancement sufficiently far away from the antenna edge (along the vertical black line in the lower left panel of Fig. S3).

The absorption spectrum of the coupled system also differs significantly from the absorption coefficient of the bare ITO (Fig. S5). Due to the stronger interaction of light with the ITO and the loss introduced by the plasmonic antennas, the absorption coefficient is higher close to the resonances of the coupled system (maximum absorption is $\sim 30\%$ within the spectral range of interest in this paper). Thus the antenna array increases the absorbed power density in the ITO film which results in the enhancement of the nonlinear response of the overall system. However, a significant fraction of the power is absorbed by the antennas which can be reduced by using dielectric antennas.

Nonlinear response of ITO

We measured the nonlinear response of the 23-nm-thick ITO sample use a Z-scan technique at normal incidence. The 23-nm-thick ITO film exhibits wavelength dependent positive nonlinear refraction and saturable absorption. The maximum value of n_2 is $\sim 1.5 \times 10^{-3}$ at $\lambda = 1400$ nm with ~ 200 GW/cm^2 incident intensity. Thus ~ 200 GW/cm^2 of incident intensity induces a change of 0.15. It can be explained, to first approximation, due to a 5% red-shift in the plasma frequency. In order to find the nonlinear response of the ITO film, we measured the nonlinear response of the ITO coated substrate (float glass) and the nonlinear response of a similar substrate seperately while keeping the incident intensity constant. We then used the relation $n_{2,\mathrm{ITO}} = (n_{2,\mathrm{ITO-with-substrate}} L_{\mathrm{ITO-with-substrate}} - n_{2,\mathrm{substrate}} L_{\mathrm{substrate}})/L_{\mathrm{ITO}}$ to find the n_2 of the ITO layer. Here, L denotes the thickness.

Refractive index homogenization

The effective linear refractive index of the medium depends on the Q-factor of the resonator and the coupling dynamics between the antennas and the ENZ film. We used the metamaterial homogenization procedure introduced by Smith et al.[17] to calculate the effective refractive index of the hybrid structure. We use the following set of equations to find both the real and the imaginary

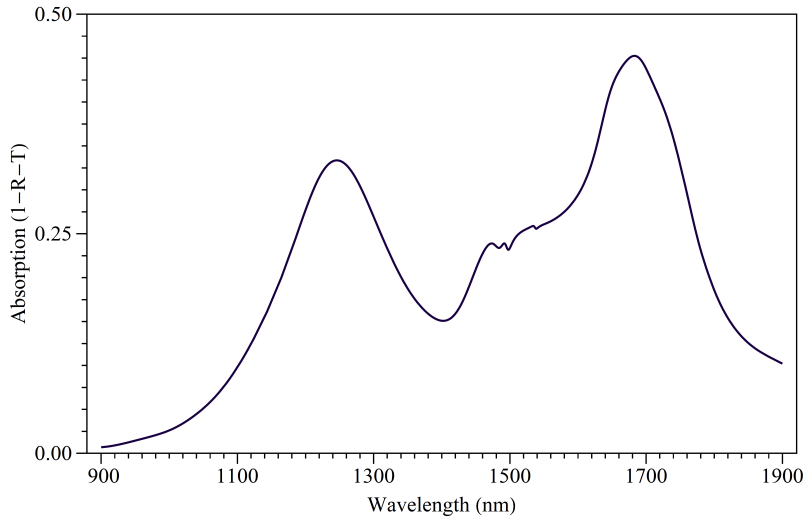

Figure S5. Absorption: Calculated absorption profile by the ITO-antenna coupled structure. The two peaks in the profile - one at a shorter wavelength than the zero-crossing wavelength and one at a larger wavelength - further confirms the strong coupling dynamics between ENZ mode and the antenna mode. Within the spectral range of interest the the theoratical maximum absorption is $\sim 34\%$.

part of the homogenized effective linear refractive index (Figure S7)

$$\begin{aligned} s_{av} &= \sqrt{s_{11}s_{22}} \\ z &= \sqrt{\frac{(1+s_{av}^2-s_{21}^2)}{(1-s_{av})^2-s_{21}^2}} \\ n_{eff} &= \frac{\imath}{2\pi d_{ITO}/\lambda}\log\left[\frac{s_{21}}{1-s_{av}\frac{z-1}{z+1}}\right] \end{aligned} \tag{14}$$

We calculated the plasma-frequency-dependent homogenized refractive index by calculating the s-parameters using a series of FDTD simulations while manually varrying the zero permittivity wavelength of the ITO film. The two-temperature model and the plasma-frequency-dependent homogenized refractive index of the overall system allows us to calculate the nonlinear refractive index of the antenna-ITO coupled system.

Change in plasma frequency and nonlinear index

To first approximation the change in the refractive index of ITO and that of the coupled system can be attributed to the red-shift of the plasma frequency as a function of incident intensity.[9,10,18,19] For example, a 5% change in the plasma frequency ($\Delta\omega_p = 5\%$) leads to a change in the refractive index of the bare ITO layer by ~ 0.16 at $\lambda = 1400$ nm which can be achieved with incident intensity of 100 GW/cm^2. Whereas, for the coupled system a red-shift of the plasma frequency leads to a much larger change in the refractive index. Depending on which spectral side of the resonance is under investigation, the change in the refractive index, Δn, can be either positive or negative. For example, in the coupled system $\Delta\omega_p = 5\%$ leads $\Delta n = -5$ and $\Delta n = 1.16$ at $\lambda = 1280$ nm and $\lambda = 1440$ nm respectively (Fig. S8). However, experimentally we measure $\Delta n_{max} \approx -2.5$ at 1280 nm and $\Delta n_{max} \approx 2.5$ at $\lambda = 1440$ nm. Thus, this simple analysis based on the red-shift of the plasma frequency overestimates the Δn_{max} on- and near- resonance but underestimates the changes far from the resonance. The change in the electronic temperature not only red-shifts the plasma frequency of the ITO but also increases the damping coefficent, i.e. the imaginary part of the permittivity. As a result, the resonance width of the coupled system broadens in addition to the red-shift of the resoance due to the change in ω_p as a function of the incident intensity. A broadened resonace of the coupled system reduces Δn_{max} at on- or near-resonance wavelengths and enhances Δn_{max} at far from resonance. The presence of the antennas thus amplify the change in the refractive index by upto a factor of 20. Moreover, the presence of the antenna introduces an intensity enhancement of at least a factor of ~ 50 at normal incidence (Fig. S4). Thus, even at the saturation intensities these two effects combined can explain a factor of 1000 enhancement of the value of n_2 of the coupled structure compared to that of the the bare ITO at $\lambda = 1400$ nm.

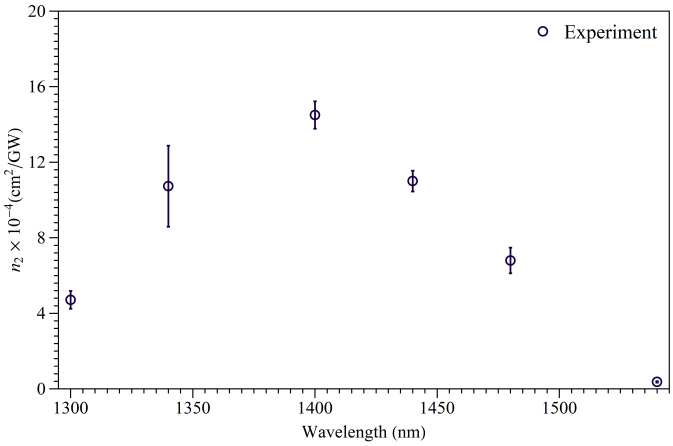

(a)

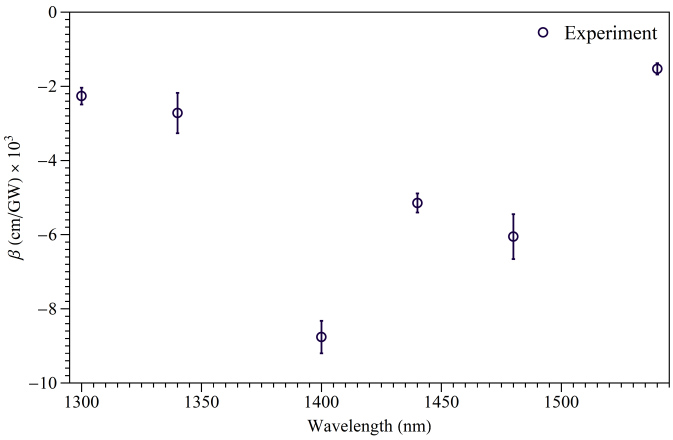

(b)

Figure S6. Measured nonlinear response of low conductivity ITO: (a) The effective nonlinear refractive index n_2 as measured using Z-scan. We use a 23-nm-thick ITO, which is used as the ENZ layer in the coupled structure, for this measurement. (b) The nonlinear absorption coefficient β.

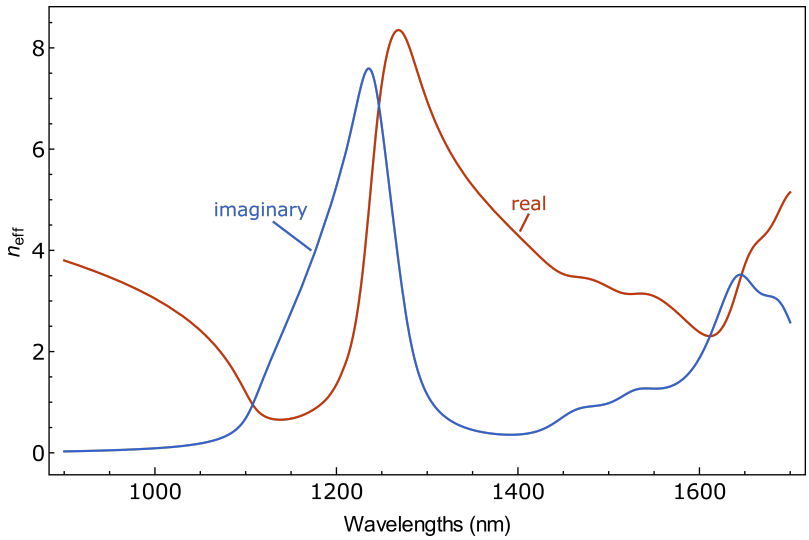

Figure S7. Homogenized refractive index: We used a refractive index homogenization technique to obtain the effective index of the antenna-ITO coupled system. The large effective nonlinear response can understood as the light induced time-dependent shift and reshaping of the homogenized linear dispersion of the coupled system.

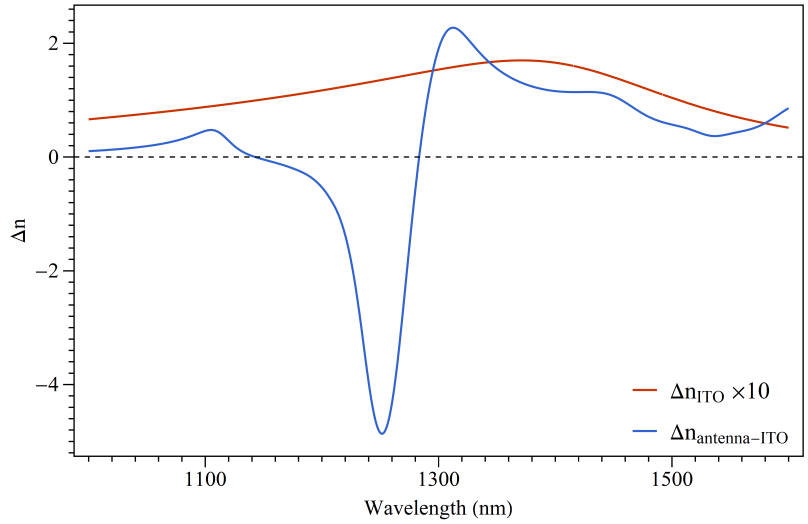

Figure S8. Change in the refractive index due to a red-shift of the plasma frequency: The plot shows that due to the presence of the antenna, a 5% change in the plasma frequency can lead to a much larger change in the refractive index in the coupled structure compared to the bare ITO. Moreover, the required incident intensity to induce a constant amount of red-shift in the plasma frequency is much smaller in the coupled structure than the bare ITO due to the field enhancement. Here, we calculate the change in the refractive index Δn simply by subtracting $\sqrt{\varepsilon(\omega_p)}$ from $\sqrt{\varepsilon(0.95\omega_p)}$. In order to calculate the refractive index for a particular plasma frequency, we use the Lorentz-Drude model and the homogenized refractive index for the bare ITO and the coupled system respectively.

Z-scan traces

We show representative Z-scan traces in the presence of large nonlinear absorption in Fig. S9a ($\lambda = 1340$nm). To obtain the nonlinear measurements, we use a pellicle beam splitter placed right after the sample to divide the beam in order to simulatenously measure closed- and open-aperture signals. We also use a reference photodiode to monitor the power fluctuation. We do two sets of measurements for each wavelength in order to calculate n_2 and β values: one set of measurements with the incident intensity low enough so that nonlinear response is absent; and the other set with an incident intensity large enough ($\sim 150\text{MW}/\text{cm}^2$) to induce a nonlinear response. We normalize the open-aperture signal by dividing the high intensity signal (normalized by the reference signal to account for the power fluctuation) by the low intensity signal (normalized by the reference signal to account for the power fluctuation). In order to find the value of the imaginary part of the phase shift we fit the normalized data to curves generated numerically, as described in the method section. For the closed-aperture signal we find the best fit after dividing the closed-aperture data by the open-aperture data. Finally, we calculate the n_2 and β values from the phase shifts using the standard equations.[20]

We perform a series of measurements with varying intensity to find the maximum possible phase shift – and the change in the refractive index – as shown in Fig. 3. We observed that for a sufficiently large incident intensities the fifth-order nonlinear effects can become important (Fig. S9b). This is the case for some of the data points in Fig. 3. In such cases, we do not divide the closed-aperture signal with the open-aperture signal in order to decouple the nonlinear refraction from the nonlinear absorption. Instead, we find the real part of the nonlinear phase shift by finding the best fit lines while taking the third- and fifth-order nonlinear absorptions into account (Fig. S9b). The phase shifts obtained with such large intensities were used to find the maximum intensity-dependent change in the refractive index (Δn) shown in Fig. 3 of the main text. The values of n_2 and β were obtained using a much lower input intensity, as mentioned above.

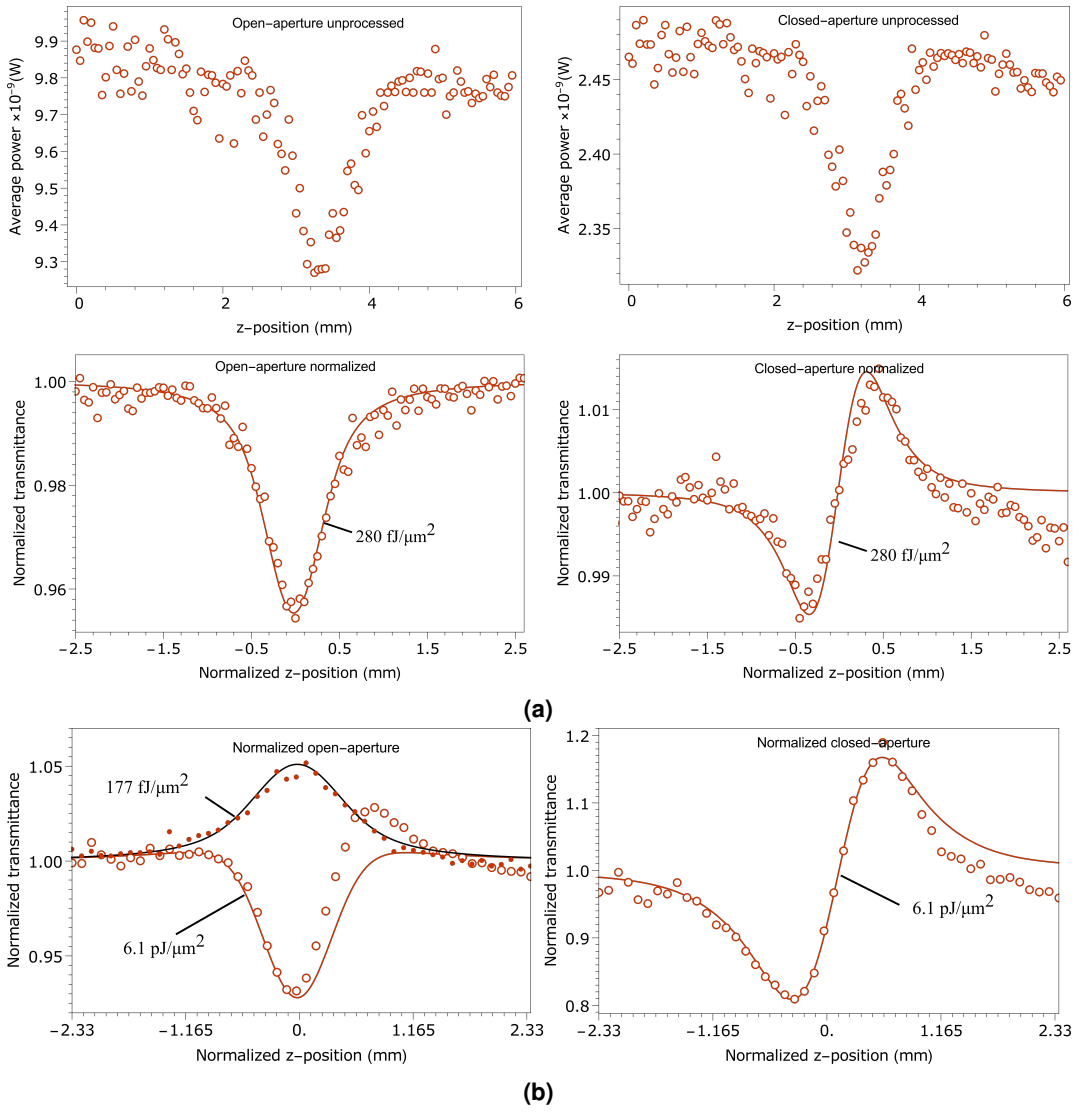

Figure S9. Z-scan traces: (a) Unprocessed (top panel) and processed data (bottom panel) for Z-scan signals at $\lambda = 1340$ nm for incident intensity of ~ 158 MW/cm^2. We obtained the normalized closed-aperture signal after dividing the closed-aperture signal with the open-aperture signal. We obtain the nonlinear phase shifts values - real phase shift = 0.055 rad and imaginary phase shift = 0.043 rad - by fitting the data with the numerically obtained curves (solid lines). (b) Normalized open- and closed-aperture signal at $\lambda = 1440$ nm for real phase shift of ~ 0.57 rad which is equivalent to $\Delta n = 2.61$. In this case, both third- and fifth-order nonlinear absorptions are important. In order to extract the phase shift from the z-scan traces, it is necessary to normalize the signal in such a way so that the transmittance far from focus approaches 1.0.

Reference	$\lvert n_2 \rvert (\text{cm}^2/\text{GW})$	λ(nm)
ITO ($R_s = 70-100\ \Omega/\text{sq.}$)[18]	4.0×10^{-5}	1000
ITO ($R_s = 8-12\ \Omega/\text{sq.}$)[18]	1.6×10^{-3}	1000
Dimer antenna-ITO[18]	5.9×10^{-2}	1000
ITO ($R_s = 4.5\ \Omega/\text{sq.}$)[19]	2.6×10^{-3}	1240
ITO ($R_s = 80\ \Omega/\text{sq.}$) (this work)	1.5×10^{-3}	1400
Dipole antenna-ITO (this work)	3.73	1240

Supplementary Table 1. Comparison of nonlinear response of ITO and hybrid ITO-antenna system at normal incidence.

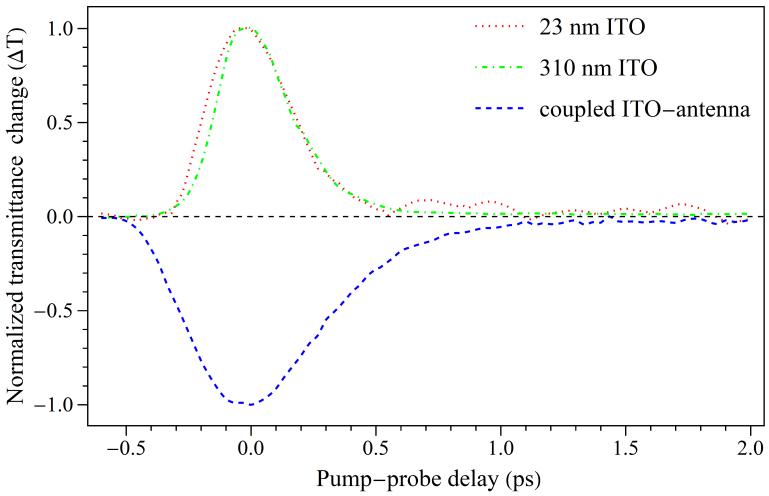

Figure S10. Response time: Normalized pump-probe transmittance of 23 nm thin ITO, 310 nm thick ITO and ITO-antenna coupled system at 1300 nm wavelength. The Pump-probe response time for the coupled system is longer than that of the thin (low conductivity) or thick (high conductivity) ITO films. We normalized the x-axis such that the zero pump-probe delay time corresponds to the maximum transmittance for visual aid.

References

1. Campione, S., Kim, I., de Ceglia, D., Keeler, G. A. & Luk, T. S. Experimental verification of epsilon-near-zero plasmon polariton modes in degenerately doped semiconductor nanolayers. *Optics Express* **24**, 18782–18789 (2016).
2. Campione, S., Brener, I. & Marquier, F. Theory of epsilon-near-zero modes in ultrathin films. *Phys. Rev. B* **91**, 121408 (2015).
3. Schulz, S. A. *et al.* Optical response of dipole antennas on an epsilon-near-zero substrate. *Physical Review A* **93**, 063846 (2016).
4. Campione, S., Wendt, J. R., Keeler, G. A. & Luk, T. S. Near-infrared strong coupling between metamaterials and epsilon-near-zero modes in degenerately doped semiconductor nanolayers. *ACS Photonics* **3**, 293–297 (2016).
5. Vassant, S. *et al.* Epsilon-near-zero mode for active optoelectronic devices. *Physical review letters* **109**, 237401 (2012).
6. Liu, X. *et al.* Quantification and impact of nonparabolicity of the conduction band of indium tin oxide on its plasmonic properties. *Applied Physics Letters* **105**, 181117 (2014).
7. Kane, E. O. Band structure of indium antimonide. *Journal of Physics and Chemistry of Solids* **1**, 249–261 (1957).
8. Chakravarti, A. & Nag, B. Generalized einstein relation for degenerate semiconductors having non-parabolic energy bands. *International Journal of Electronics Theoretical and Experimental* **37**, 281–284 (1974).
9. Guo, P., Schaller, R. D., Ketterson, J. B. & Chang, R. P. H. Ultrafast switching of tunable infrared plasmons in indium tin oxide nanorod arrays with large absolute amplitude. *Nature Photonics* **10**, 267–273 (2016).
10. Guo, P. *et al.* Large optical nonlinearity of ito nanorods for sub-picosecond all-optical modulation of the full-visible spectrum. *Nature Communications* **7**, 12892 (2016).
11. Brorson, S., Fujimoto, J. & Ippen, E. Femtosecond electronic heat-transport dynamics in thin gold films. *Physical Review Letters* **59**, 1962 (1987).
12. Sun, C.-K., Vallee, F., Acioli, L., Ippen, E. & Fujimoto, J. Femtosecond investigation of electron thermalization in gold. *Physical Review B* **48**, 12365 (1993).
13. Carpene, E. Ultrafast laser irradiation of metals: Beyond the two-temperature model. *Physical Review B* **74**, 024301 (2006).
14. Lin, Z., Zhigilei, L. V. & Celli, V. Electron-phonon coupling and electron heat capacity of metals under conditions of strong electron-phonon nonequilibrium. *Physical Review B* **77**, 075133 (2008).
15. Yagi, T. *et al.* Analysis on thermal properties of tin doped indium oxide films by picosecond thermoreflectance measurement. *Journal of Vacuum Science & Technology A* **23**, 1180–1186 (2005).

16. Voisin, C., Fatti, N. D., Christofilos, D. & Vallée, F. Ultrafast electron dynamics and optical nonlinearities in metal nanoparticles. *The Journal of Physical Chemistry B* **105**, 2264–2280 (2001).

17. Smith, D. R., Schultz, S., Markoš, P. & Soukoulis, C. Determination of effective permittivity and permeability of metamaterials from reflection and transmission coefficients. *Physical Review B* **65**, 195104 (2002).

18. Abb, M., Albella, P., Aizpurua, J. & Muskens, O. L. All-optical control of a single plasmonic nanoantenna–ito hybrid. *Nano letters* **11**, 2457–2463 (2011).

19. Alam, M. Z., De Leon, I. & Boyd, R. W. Large optical nonlinearity of indium tin oxide in its epsilon-near-zero region. *Science* **352**, 795–797 (2016).

20. Sheik-Bahae, M., Said, A. A., Wei, T.-H., Hagan, D. J. & Van Stryland, E. W. Sensitive measurement of optical nonlinearities using a single beam. *IEEE Journal of Quantum Electronics* **26**, 760–769 (1990).